Title

iRGD-Targeted Physalis Mottle Virus Like Nanoparticles for Targeted Cancer Delivery

Authors

Barkovich, Krister J
Zhao, Zhongchao
Steinmetz, Nicole F

Publication Date

2023

DOI

10.1002/smsc.202300067

iRGD-targeted Physalis Mottle Virus-like Nanoparticles for Targeted Cancer Delivery

Krister J. Barkovich[1], Zhongchao Zhao[2,3], Nicole F. Steinmetz[1,2,3,4,5,6,7*]*

[1] Department of Radiology, University of California, San Diego, San Diego, CA
[2] Department of NanoEngineering, University of California, San Diego, San Diego, CA
[3] Center for Nano-ImmunoEngineering, University of California, San Diego, San Diego, CA
[4] Department of Bioengineering, University of California, San Diego, San Diego, CA
[5] Institute for Materials Discovery and Design, University of California, San Diego, CA
[6] Moores Cancer Center, University of California, San Diego, San Diego, CA
[7] Center for Engineering in Cancer, Institute for Engineering in Medicine, University of California, San Diego, San Diego, CA

**co-corresponding: kbarkovich@health.ucsd.edu and nsteinmetz@ucsd.edu*

Abstract

Nanomedicine provides a promising platform for the molecular treatment of disease. An ongoing challenge in nanomedicine is the targeted delivery of intravenously administered nanoparticles to particular tissues, which is of special interest in cancer. In this study, we show that the conjugation of iRGD peptides, which specifically target tumor neovasculature, to the surface of Physalis mottle virus (PhMV)-like nanoparticles leads to rapid cellular uptake *in vitro* and tumor homing *in vivo*. We then show that iRGD-targeted PhMV loaded with the chemotherapeutic doxorubicin shows increased potency in a murine flank xenograft model of cancer. Our results validate that PhMV-like nanoparticles can be targeted to tumors through iRGD-peptide conjugation and suggest that iRGD-PhMV provides a promising platform for the targeted delivery of molecular cargo to tumors.

Introduction

Cancer is the second leading cause of death in the United States, causing greater than 600,000 deaths in 2020.[1] Our growing understanding of the molecular mechanisms of cancer has led to an ever-expanding arsenal of molecular targeted therapy. However, the clinical translation of many promising therapies has been hampered by poor efficacy, toxicity, and off-target effects, perhaps due to imprecise delivery of these therapeutics to the tissue or organ of interest.[2,3] As generalizable strategies for the targeted delivery of cargo to specific tissues remains a challenge, there is increasing research into the use of nanomaterials as carriers for targeted delivery of chemotherapeutics, synthetic nucleic acids, and imaging reagents to tumors.[4,5] While data demonstrate tumor homing of nanoparticles (NPs) through various targeting approaches, a meta-analysis of the data indicates that only 0.7% of intravascularly administered NPs are delivered to

solid tumors.[6] Hurdles to tissue-specific delivery of NPs are numerous and include non-specific uptake by the mononuclear phagocyte system (MPS) and endothelial and cellular barriers at the tumor.[7]

Multiple different nanocarrier platforms are currently under development and include lipid-based, polymeric, and inorganic NPs, as well as naturally occurring and engineered viruses or viral vectors,[8] each of which has its own advantages and disadvantages in terms of carrying capacity, biodistribution, and facility of manipulation.[9] In comparison with synthetic NPs, viral NPs are protein-based nanostructures with high biocompatibility (i.e. when using non-infectious viruses), structural uniformity, and ease of synthesis and manipulation through cell culture, fermentation, or molecular farming.[10] Virus-like particles (VLPs), proteinaceous NPs derived from the coat protein of viral capsids, lack the genomic nucleic acids of other viral NPs and are therefore non-infectious.[11] While the immunogenicity and safety concerns for mammalian virus-based nanoparticles has limited the translation of these technologies into the clinic, plant virus NPs and VLPs are an emerging alternative.[12] Virus-based NPs can be easily functionalized through genetic manipulation and reactive amino acids to carry chemotherapeutics, synthetic genes, and imaging reagents,[13-15] and functionalized to tune pharmacokinetics.[16] Therefore in this work, we turned toward the study of a plant VLP, engineered to home to tumors. While the aforementioned meta-analysis was very comprehensive, it lacked the analysis of data for VLPs or viral vectors. To fill this gap in knowledge we chose a plant VLP combined with a universal targeting strategy. Specifically, we used VLPs derived from the plant virus *Physalis mottle virus* (PhMV), a +ssRNA virus from the family *Tymoviridae* that forms a ~30 nm-sized icosahedral capsid from 180 identical coat proteins, and can be expressed and purified from *Escherichia coli*

as a monodisperse and stable VLP.[17] PhMV VLPs can be functionalized internally with chemotherapeutics and imaging reagents[18] and externally with targeting peptides.[19]

One of the six hallmarks of cancer is sustained angiogenesis,[20] the process by which new capillaries sprout and branch from existing vasculature.[21] In adults, there are few tissues with physiologic angiogenesis, so this molecular signature is relatively specific for malignancy and injured tissues.[22] As such, tumors can be targeted with relative specificity by directing NPs towards new vasculature, and several biologics targeting this process have been FDA-approved for the treatment of metastatic GI malignancies and renal cell carcinoma.[23] Peptides with an arginine-glycine-aspartate (RGD)-motif have been shown to display high affinity for $\alpha v\beta 3$ and 5 integrins, which are upregulated on angiogenic endothelial cells.[24] The iRGD peptide, which includes a C-end rule (CendR) motif within a cyclic RGD peptide, undergoes a proteolytic cleavage to reveal a neuropilin-1 (NRP-1) binding fragment that stimulates uptake within the tumor stroma.[25] Cyclic RGD and iRGD peptides have been used for delivery of a wide range of cargo to tumor models, including therapeutics, nanoparticles, and imaging reagents.[26-28] Data from other nanoparticle systems indicate that conjugation to iRGD peptides leads to a two- to eight-fold increase in tumor localization of oncolytic adenovirus NPs and aggregated albumin-based NPs, respectively, [25,29] although increased intratumoral localization of lipid bilayer-coated silica NPs was not seen with iRGD conjugation [28]. Here, we assess if iRGD-peptides can be used for targeted delivery of PhMV VLPs to tumors. Specifically, we analyze whether iRGD-PhMV VLPs are taken up by cells *in vitro* and show increased intratumoral localization *in vivo*. We then evaluate if iRGD-PhMV VLPs loaded with the chemotherapeutic doxorubicin can be used for targeted cancer treatment.

Experimental

Preparation of PhMV VLPs. PhMV VLPs were prepared by expressing the coat protein in BL21(DE3) as previously described.[18] Briefly, BL21(DE3) were transformed with pRSETa-PhMV CP. A single colony was isolated and used to inoculate 50 mL of Luria Broth (LB, Sigma) supplemented with carbenicillin at 50 μg/mL, and grown overnight at 37 ºC. This was used to inoculate 1 L of terrific broth (TB, Sigma Aldrich) supplemented with carbenicillin at a 1:100 dilution. Cultures were grown at 37 ºC to OD_{600} ~ 1.0 and induced with 0.5 mM IPTG (Sigma) at 30 ºC overnight. Cultures were then pelleted, lysed by sonication in 50 mM sodium citrate pH 5.5 (SCB) and clarified at 30,000 x g for 30 min at 4 ºC. VLPs were precipitated using 10 % (w/v) polyethylene glycol (PEG), resuspended in SCB, then purified by ultracentrifugation using a 50.2 Ti rotor at 35,000 rpm for 3 hours at 4 ºC. Pellets were resuspended overnight in SCB then layered onto a 10-40% linear sucrose gradient and separated using a SW32 rotor at 28,000 rpm for 3 hours at 4 ºC. The light scattering zone was collected, diluted with SCB, and centrifuged at 42,000 rpm for 3 hours at 4 ºC using a 50.2 Ti rotor. The final pellet was resuspended in SCB to yield the pure VLP, which was stored at 4 ºC. Protein concentration was determined by BCA Assay (Thermo Fisher) using BSA as a standard.

Bioconjugation reactions. Internal cysteines residues of PhMV particles (at 1.5 mg/mL) in 10 mM potassium phosphate (KP) pH 7.5 were alkylated using maleimide-sulfoCy5 (LumiProbe) at 3 molar equivalents per coat protein (eq/CP) or aldoxorubicin (Aldox, MedChem Express) at 5 eq/CP at room temperature overnight. The resulting product was purified by ultracentrifugation

(121,139 x g, 70 min, 4 ºC over a sucrose cushion (30% sucrose). The pellet was dissolved in 10 mM KP pH 7.5 and used for further bioconjugation reactions. External lysine residues of PhMV particles (at 1.5 mg/mL) in 10 mM KP pH 7.5 were acylated using NHS esters (NHS-PEG4-N_3, NHS-PEG2K, or NHS-PEG2K-maleimide) (Nanocs) at 50 eq/CP for 3 hours at room temperature followed by purification by ultracentrifugation as above. Copper-catalyzed azide-alkyne cycloaddition (CuAAC) reactions were performed using N_3-PhMV-Cy5 or N_3-PhMV-Aldox (at 1 mg/mL) in 10 mM KP pH 7.0; particles were reacted with 1 mM $CuSO_4$ (Sigma), 200 μM tris-hydroxypropyltriazolylmethylamine (THPTA, Click Chemistry Tools), 5 mM aminoguanidine (AMG, Sigma), and 5 mM sodium ascorbate (Sigma) with 1 eq/CP propargylglycine-aminohexanoic acid-iRGD (Pra-iRGD), unless otherwise noted, for 1hr at room temperature and purified by ultracentrifugation, as above ($CuSO_4$, THPTA, AMG, and sodium ascorbate were pre-mixed as a 10x master mix, then added to PhMV particles prior to the addition of Pra-iRGD). Two eq/CP fluorescein-Cys-aminohexanoic acid-iRGD (FAM-Cys-iRGD) was conjugated to Mal-PhMV-Cy5 or Mal-PhMV-Aldox at 1 mg/mL in 10 mM KP pH 7.5 at room temperature overnight, quenched with 100 eq/CP beta-mercaptoethanol (Sigma) at room temperature for one hour, and purified by ultracentrifugation, as above. Final particles were buffer exchanged into PBS, concentrated to >5 mg/mL, passed through a 0.22 μm filter, and stored at 4 ºC and used within two weeks of synthesis. Concentration was determined by BCA assay (ThermoFisher) using BSA as a standard.

Particle characterization. Final particles were characterized by SDS-PAGE (12% Bis-Tris (Novex, ThermoFisher), native gel electrophoresis (0.8% w/v agarose in TBE), UV-Vis (Nanodrop 200 spectrophotometer, ThermoFisher), size exclusion chromatography (Superose 6

Increase 10/300 GL column at 0.5 mL/min on a AKTA FPLC, GE), dynamic light scattering (Zetasizer Nano ZSP/Zen5600, Malvern Panalytical), and transmission electron microscopy with 400-mesh hexagonal copper grids using UAc-negative-staining (2% w/v) and a FEI TecnaiSpirit G2 BioTWIN TEM at 80 kV for image acquisition, as applicable. The concentration of PhMV-bound sulfo-Cy5, doxorubicin, and FAM-Cys-iRGD was determined by UV-Vis spectroscopy using the extinction coefficients e(sulfo-Cy5, 646 nm) = 271,000 $M^{-1}cm^{-1}$, e(DOX, 488 nm) = 11,500 $M^{-1}cm^{-1}$, and e(FAM, 495 nm) = 20960 $M^{-1}cm^{-1}$.

Integrin-binding ELISA. Ninety-six well plates (MaxiSorp, ThermoFisher) were incubated with 0.5 μg/mL recombinant αvβ3 integrin (R&D Systems) in 100mM KP pH 8.0 at 4ºC overnight. Plates were then blocked with 5% (w/v) bovine serum albumin (BSA, Sigma) in PBS supplemented with 1 mM $CaCl_2$, 0.5 mM $MgCl_2$, and 0.1% (v/v) Tween-20 (PBSD-T). Plates were then incubated for 90 min at room temperature with serial dilutions of PhMV VLPs (25 nM -> 1.6 pM) in 2% (w/v) BSA/PBSD-T. Plates were then washed with PBSD-T, incubated with rabbit anti-PhMV primary antibodies (1:1000, Pacific Immunology) in 5% (w/v) BSA/PBSD-T followed by HRP-conjugated goat anti-rabbit secondary antibodies (1:5000, ThermoFisher). Plates were then developed using TMB-ELISA substrate (ThermoFisher) and absorbance was measured at 450 nm. All conditions were performed in triplicate. Curves were fit using at least-squares method (Prism, GraphPad).

Flow cytometry. A2780 cells were grown to approximately 75% confluence in RPMI media (Corning) supplemented with 10% (v/v) fetal bovine serum (FBS, R&D Systems) and 1% (v/v) penicillin-streptomycin (Cytiva) at 37ºC in a 5% CO_2 humidified incubator. Cells were isolated

using non-enzymatic cell dissociation buffer (Gibco) and resuspended at 1.0 x 10^7 cells/mL in RPMI. Cells were incubated with 2.5 x 10^6 particles/cell for the specified time (5 – 60 min), washed three times with ice-cold PBS, then analyzed for internal fluorescence using the APC channel (Cy5 particles) or PE channel (Aldox particles) on an Accuri C6 Plus (BD Biosciences). At least 10,000 live events were acquired per sample, and all conditions were performed in triplicate. Results were analyzed with FlowJo (BD Biosciences) and statistical significant determined by student's t-test (Prism, GraphPad).

Confocal microscopy. A2780 cells were plated at 25,000 cells/well in a 24 well plate on circular glass coverslips and grown overnight using the above growth conditions. PhMV particles were added directly to the media at 2.5 x 10^6 particles/cell for 10 minutes. Cells were then transferred to 4ºC, washed with cold PBS, and fixed with fixation buffer (4% paraformaldehyde, 0.3% glutaraldehyde in PBS) for 5 min at room temperature. Cells were then stained with wheat-germ agglutinin-Alexa Fluor 488 (WGA; Sigma) in 5% BSA/PBS and mounted on glass slides using Fluoroshield with DAPI (Sigma). Slides were then analyzed on a A1R confocal microscope (Nikon). Image analysis and final images were created using Fiji (NIH).[30]

Doxorubicin release assay. PhMV-Aldox particles at 2 mg/mL in micro-dialysis chambers (ThermoFisher) were incubated in PBS (pH 7.4) or 50mM sodium citrate (pH 5.5) and doxorubicin release was measured by plate reader (excitation 488 nm, emission 595 nm), as previously described.[31]

Cytotoxicity assay. A2780 cells were plated at 3,000 cells/well in 96 well plates and grown overnight using the above growth conditions. Serial dilutions (20 μM -> 1.3 nM) of doxorubicin or PhMV-Aldox particles (normalized to doxorubicin concentration) were added and plates were incubated for 72 hours. Viable cells were then analyzed using a CellTiter Glo assay (Promega) according to the manufacture's protocol. All conditions were performed in triplicate. Curves were fit using a least-squares methods (Prism, GraphPad).

***In vivo* biodistribution study.** All animal experiments were carried out according to IACUC-approved procedures at the University of California, San Diego. Mice were anesthetized for all procedures (2.5% isoflurane, O_2 flow 2.0 L/min). Mice were maintained on an alfalfa-free (low fluorescence) diet (2018S Teklad, Envigo). A2780 cells were grown to 75% confluence using the above growth conditions, harvested using Trypsin-EDTA (Corning) and injected subcutaneously at a concentration of 2 x 10^6 cells/mL in a 1:1 mixture of RPMI:Matrigel (Corning) into the flank of female BALB/c Nu/Nu mice at 4-6 weeks of age. After 10 days, tumor-bearing mice were allocated into one of four treatment groups (PBS, PEG2K-PhMV-Cy5, PEG2K-PhMV-Cy5 + 4 μmol/kg iRGD, or iRGD-PEG2K-PhMV-Cy5; n = 5 per group) and intravenously dosed with 200μg PhMV particles in 100μL PBS via tail vein. For *in vivo* NIRF imaging, mice were scanned at approximately 4, 8, 24, 48, 72, 96, 120 hours after injection using an IVIS 200 small-animal imaging system (Xenogen, using Cy5.5 excitation and emission filters). After the final NIRF imaging, mice were euthanized and the tumor and major organs were removed and imaged for *ex vivo* fluorescence. The tissues were then weighed and homogenized and analyzed for fluorescence using a plate reader (Tecan).

***In vivo* treatment study.** MDA-MB-231 cells were grown in DMEM (Corning) supplemented with 10% FBS and 1% pen/strep, harvested using Trypsin-EDTA (Corning) and injected subcutaneously at a concentration of 1 x 10^6 cells/mL in a 1:1 mixture of RPMI:Matrigel (Corning) into the flank of female BALB/c Nu/Nu mice at 4-6 weeks of age, as previously described.[31] Tumor-bearing mice were allocated into one of four treatment groups (PBS, PEG2K-PhMV-Aldox, PEG2K-PhMV-Aldox + 4 μmol/kg iRGD, or iRGD-PEG2K-PhMV-Aldox) when tumor volume reached ~100 mm^3. The mice were intravenously injected twice per week with the appropriate treatment at a dosage of 0.5 mg doxorubicin per kg body weight. Treatments were stopped after nine doses (39 days post injection). Tumor size and body weight were measured before each injection and twice weekly afterwards, and total tumor volume was calculated using the formula $V = l \times w^2/2$. Mice were euthanized when tumor volume reached 1000 mm^3 according to IACUC guidelines.

Results

Preparation and characterization of iRGD-conjugated PhMV nanoparticles. PhMV-like nanoparticles were prepared by expressing the PhMV coat protein in *E. coli*, as previously described,[18] and were found to be monodisperse and homogenous (Figure S1). To conjugate iRGD peptides to the external surface of PhMV, we functionalized the external lysines with a bifunctional NHS-ester-azide linker that was coupled to iRGD functionalized with an N-terminal propargylglycine through copper (I)-catalyzed azide-alkyne cycloaddition[32,33] (Figure 1A). The internal compartment of PhMV was loaded with the near-IR fluorescence (NIRF) dye sulfo-Cy5 using maleimide-cysteine chemistry to allow for NP tracking by fluorescence imaging (Figure 1B). Conditions were selected to load a small quantity of dye per coat protein to avoid internal

fluorescence quenching,[18] and denatured coat proteins and whole particles showed robust NIRF fluorescence (Figure 1C-D). PhMV VLPs offer 180 internal cysteines and 720 external lysines for bioconjugation; based on absorbance measurements approximately 10 sulfo-Cy5 dyes were conjugated per VLP; at this density quenching but providing sufficient signal for imaging. Native gel electrophoresis, SDS-PAGE, and SEC confirmed covalent attachment of the dye as Cy5 co-migrated with VLPs or denatured coat proteins (Figure 1C-E).

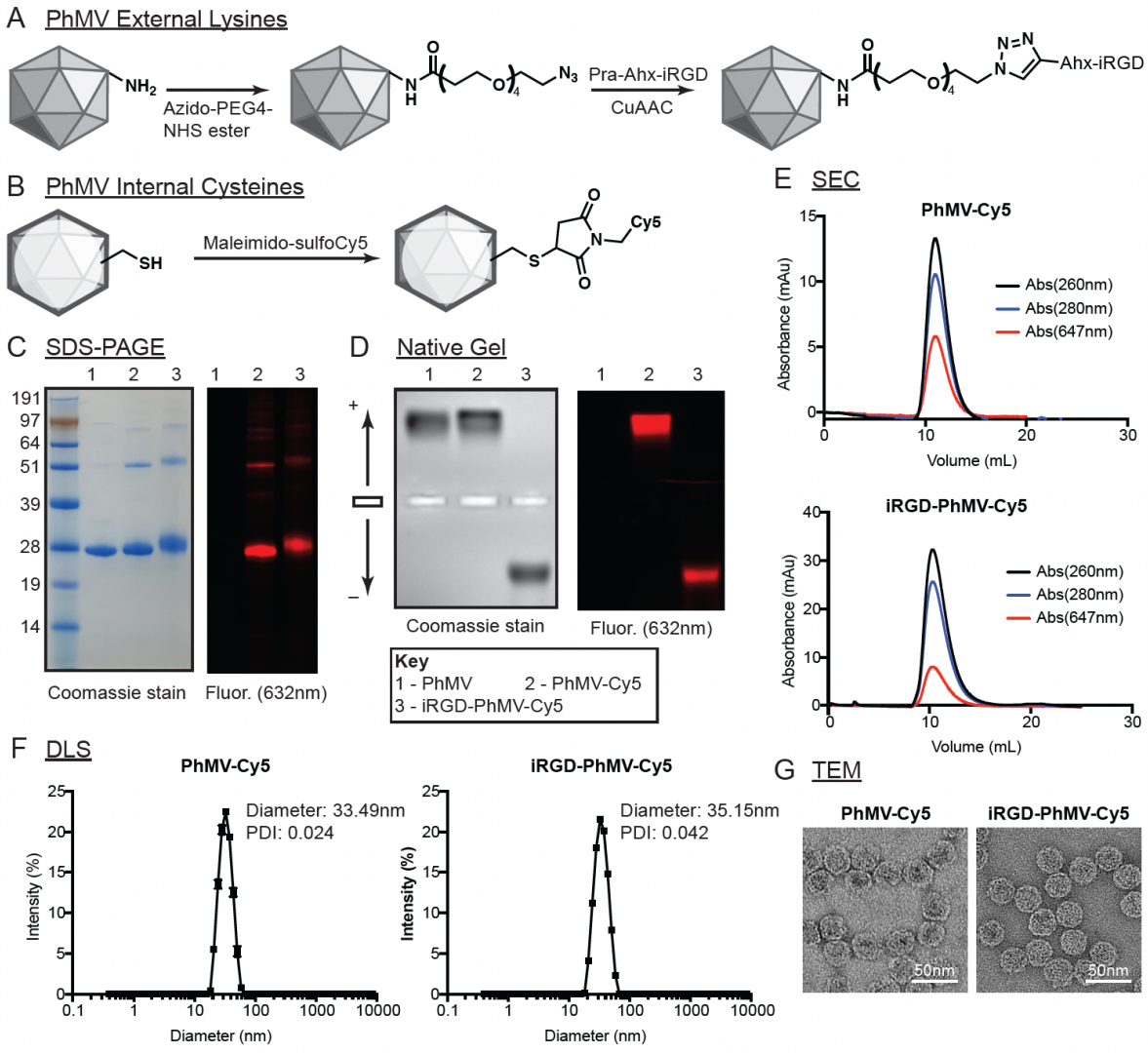

Figure 1. Synthesis of PhMV-IRGD conjugates. A. Scheme for conjugation of iRGD to the external lysines of PhMV using NHS-ester chemisty and Copper (I)-catalyzed azide-alkyne cycloaddition (CuAAC). B. Scheme for

conjugation of sulfoCy5 to internal cysteines of PhMV using maleimide chemistry. C-G. Characterization of iRGD-PhMV-Cy5 and PhMV-Cy5 using SDS-PAGE (C), native gel electrophoresis (D), size-exclusion chromatography (E), dynamic-light scattering (F), and transmission electron microscopy (G).

The final product, iRGD-PhMV-Cy5 (and an iRGD-free control, PhMV-Cy5), was structurally sound and overall matched the NP characteristics of the unmodified VLPs. Monodisperse and homogenous NP preparations of iRGD-PhMV-Cy5 were detected by native gel electrophoresis, size-exclusion chromatography (SEC), and dynamic light scattering (DLS) (Figure 1D-F). SEC showed the characteristic elution profile (~11 mL from Superose 6 Increase 10/300 GL column) with Cy5 and VLP co-eluting; aggregation, broken VLPs, or free CP was not detected. DLS and TEM were in agreement showing NPs measuring ~ 30 nm in diameter. Transmission electron microscopy was used to confirm the structural integrity of the nanoparticles (Figure 1G). The marked mobility change between PhMV VLPs and iRGD-PhMV-Cy5 by native gel electrophoresis (Figure 1D) is explained by the neutralization of surface lysines through reaction with the NHS-ester-azide linker.

The amount of iRGD peptide loaded onto PhMV could be altered by adjusting the molar ratio of peptide per PhMV coat protein (Figure S2), with a near linear relationship observed at low concentration (Figure S2B-C). Therefore, we also generated a set of nanoparticles with a range of concentration of surface-bound iRGD peptides: in addition to iRGD-PhMV-Cy5, which was synthesized using an equimolar ratio of iRGD peptide to PhMV coat proteins, we also generated particles with 0.5 and 2.0 iRGD peptides per coat protein, referred to as iRGD-PhMV-Cy5-0.5 and iRGD-PhMV-Cy5-2.0, respectively (Figure S3).

αv integrin binding properties of iRGD-PhMV nanoparticles. An enzyme-linked immunosorbent assay (ELISA) was next performed to assess whether the iRGD peptides on the surface of PhMV VLPs were appropriately positioned and maintained affinity for αv integrins (Figure 2A). iRGD-PhMV-Cy5 NPs bound αvβ3 integrins with picomolar affinity (Figure 2B). This affinity was dose dependent with the surface concentration of iRGD peptide, and iRGD-PhMV-Cy5-2.0 displayed a sub-100 pM affinity for αvβ3 integrin, while non-iRGD functionalized NPs show minimal binding.

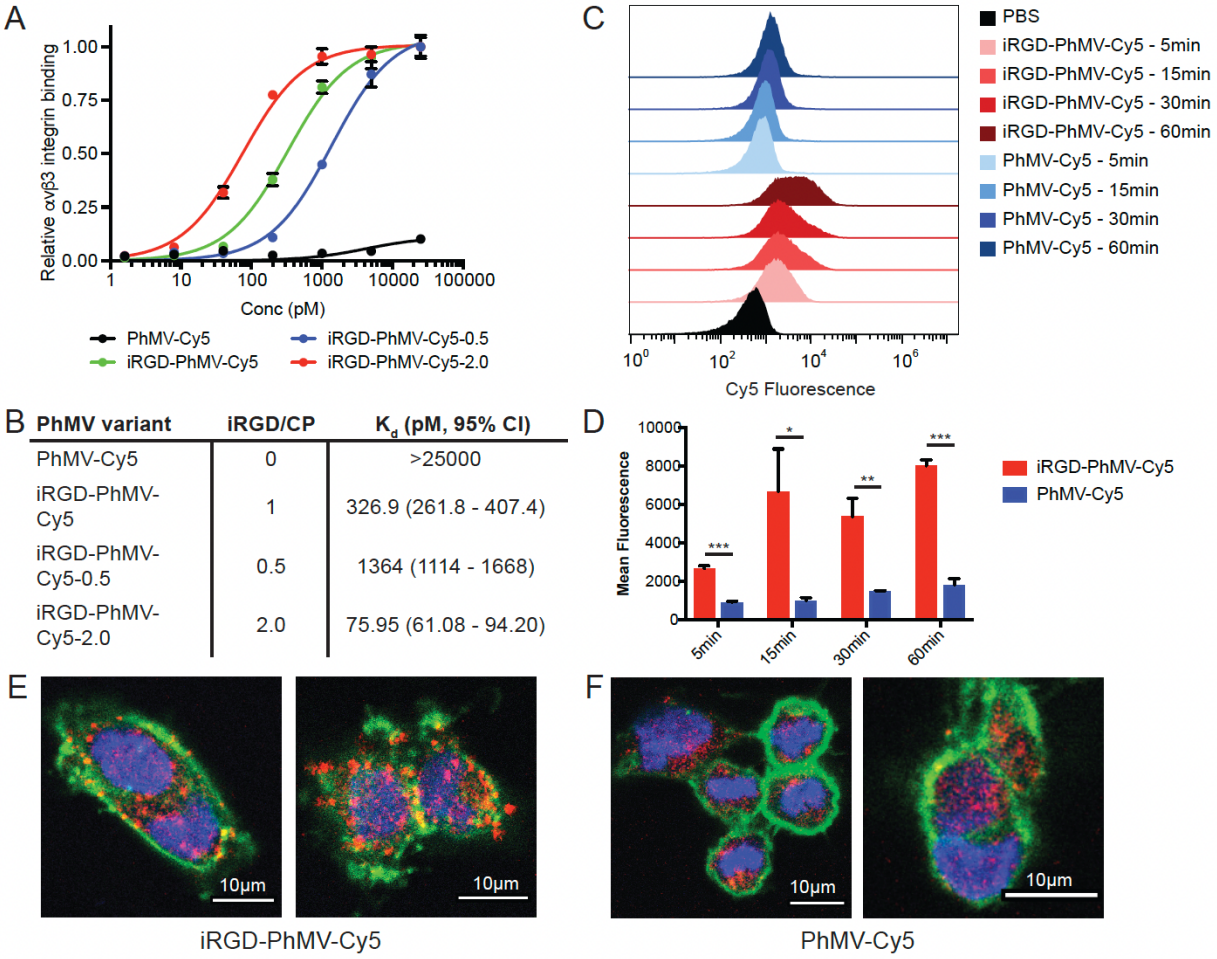

Figure 2. iRGD-PhMV binds tightly to αvβ3 integrins and is rapidly taken up by A2780 cells. A-B. Binding curves (A) and calculated Kd (B) of iRGD-PhMV-Cy5 panel in αvβ3 integrin-binding ELISA. C-D.

iRGD-PhMV-Cy5 uptake by A2780 cells after 5, 15, 30, and 60 minutes, as measured by flow cytometry (C) with quantification (D). E-F. Confocal imaging of A2780 cells after 10 minute incubation with iRGD-PhMV-Cy5 (E) or PhMV-Cy5 (F). Error bars represent S.E.M. of three replicates. Statistical analysis by two-tailed t-test (*: $p<0.05$, **: $p<0.01$, ***: $p<0.001$).

Cancer cell binding properties of iRGD-PhMV nanoparticles. PhMV VLPs have previously been shown to be internalized by cultured cells through endocytosis into the endolysosomal compartment.[18] To assess whether iRGD peptide conjugation to the VLPs alters the rate or fate of cellular uptake of the VLPs, A2780 cells were incubated with iRGD-PhMV-Cy5 or PhMV-Cy5 and analyzed using flow cytometry. We observed a five-fold increase in the level of uptake of iRGD-conjugated PhMV as compared to control at all timepoints under one hour (Figure 2C-D). A two-fold increase or decrease in RGD-peptide concentration on the VLP surface does not significantly change this rate of uptake (Figure S4). To assess if the increased rate of uptake of iRGD-conjugated PhMV is related to changes in the mechanism of uptake, we performed confocal microscopy with nuclear staining using DAPI and cell surface staining using fluorescently labeled wheat-germ agglutinin (Figure S5). Whereas PhMV-Cy5 particles are seen in the endolysosomal compartment, iRGD-PhMV-Cy5 particles are clustered in punctate foci adjacent to the plasma membrane (Figure 2E-F).

Preparation and characterization of PEGylated iRGD-PhMV nanoparticles. Our group and others have shown that the addition of polyethylene glycol (PEG) to the surface of viral nanoparticles can reduce immune clearance and improve pharmacokinetics,[16] which is consistent with synthetic NP formulations. [34] In our previous work with PhMV VLPs, we utilized a 2000 Da PEG (PEG2K) coating and hence we adapted these methods here. We generated iRGD-conjugated PEG2K-PhMV NPs by conjugating maleimide-PEG2K-NHS esters to the surface

296 lysines of PhMV, and then linking fluorescein-cysteine-aminohexanoic acid-iRGD (FAM-Cys-
297 iRGD) using thiol-maleimide chemistry (Figure S6A). A PEGylated iRGD-free control, PEG2K-
298 PhMV-Cy5, was also synthesized. Again, the final product, iRGD-PEG2K-PhMV-Cy5 remained
299 structurally sound (Figure S6B-G). Based on gel migration by SDS-PAGE, approximately half of
300 all PhMV CPs were conjugated to PEG2K, corresponding to approximately 90 PEG2K
301 molecules per VLP. Based on absorbance measurements, ~17 FAM-Cys-Ahx-IRGD were
302 conjugated per VLP. iRGD-PEG2K-PhMV-Cy5 binds αvβ3 integrin with affinities similar to
303 that of iRGD-PhMV-Cy5, indicating preserved structure and function of surface-bound iRGD
304 peptides (Figure S7A-B).
305
306 ***In vivo* biodistribution of iRGD-PhMV nanoparticles.** To assess whether iRGD-conjugated
307 PhMV NPs home to tumors *in vivo*, we next analyzed the biodistribution of iRGD-PEG2K-
308 PhMV-Cy5 using an A2780 xenograft tumor model in Nu/Nu BALB/c mice (Figure 3A). After
309 tumors were established, 200 μg of iRGD-PEG2K-PhMV-Cy5 was injected intravenously
310 through the tail vein. Since it has been previously shown that co-administration of iRGD peptide
311 with small molecules and inorganic nanoparticles can induce a similar increase in tumor uptake
312 as compared to direct iRGD peptide conjugation (the so-called 'bystander effect'),[26] 200 μg of
313 PEG2K-PhMV-Cy5 was also co-administered with 4 μmol/kg free iRGD peptide. PEG2K-
314 PhMV-Cy5 was used as a control. *In vivo* NIR fluorescence was measured four and eight hours
315 after nanoparticle injection, then daily for seven days. After administration, intratumoral NIR
316 fluorescence peaked after 48-72 hours (Figure 3B). There was a 64%, 47%, and 25% increase in
317 intratumoral fluorescence in iRGD-PEG2K-PhMV-Cy5 treated mice after 1, 2, and 3 days,
318 respectively, as compared to control, as well as a 47%, 36%, and 22% increase with iRGD

coadministration as compared to PhMV lacking conjugated or co-administered iRGD, indicated increased tumoral PhMV nanoparticle uptake in these conditions. Representative *in vivo* NIRF images show there is also significant non-specific nanoparticle uptake in the liver and spleen (Figure 3C), with complete data in supplemental figure S8. Six days after injection, the animals were euthanized and *ex vivo* NIRF analysis of the tumors and major organs was performed. There is a trend towards, but no statistically significant difference between *ex vivo* tumor NIRF signal at this timepoint. There is no statistically significant difference in splenic or hepatic uptake between iRGD-conjugated PhMV nanoparticles and non-targeted controls (Figure 3D, Figure S8B-E). Overall data show tumor homing of the VLPs with increased tumor accumulation of iRGD formulations either by conjugation to or co-administration with the VLPs.

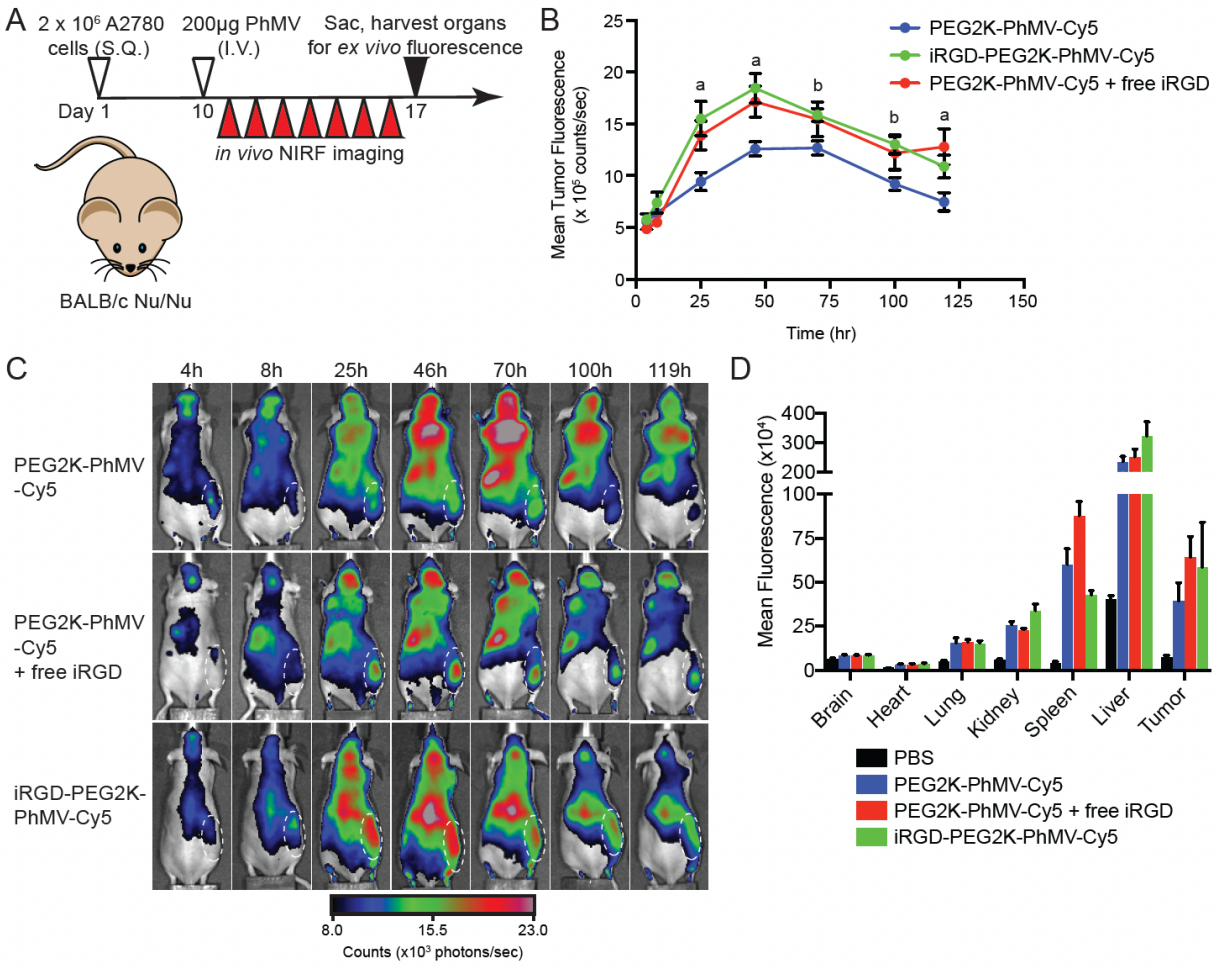

Figure 3. Conjugation or co-administration of iRGD increases uptake of PhMV in A2780 xenograft model. A. A2780 cells were injected subcutaneously into BALB/c Nu/Nu mice on day 1 followed by intravenous administration of PBS, PEG2K-PhMV-Cy5, PEG2K-PhMV-Cy5 + 4mmol/kg iRGD peptide, or iRGD-PEG2K-PhMV-Cy5 on day 10. Mice are imaged daily using in vivo NIRF imaging for 7 days, then sacrificed and organs are analyzed for ex vivo fluorescence. B-C. Quantified in vivo fluorescence of mice treated with Cy5-PhMV panel (B) and representative images (C). D. Ex vivo fluorescence of mouse organs and tumor. Error bars represent S.E.M. Statistical analysis by two-tailed t-test (ns: not significant, a: $p<0.05$ for iRGD-PEG2K-PhMV-Cy5 and PEG2K-PhMV-Cy5 + free iRGD, b: $p<0.05$ for iRGD-PEG2K-PhMV-Cy5).

Preparation and characterization of doxorubicin-loaded iRGD-PhMV nanoparticles. We have previously shown that the chemotherapeutic doxorubicin can be conjugated to PhMV nanoparticles through thiol-maleimide chemistry using its derivative aldoxorubicin (Figure

4A).[31] The hydrazone linker of aldoxorubicin is designed to release free doxorubicin within the acidic tumor microenvironment and/or the endolysosomal compartment of tumor cells.[35] PhMV was loaded with aldoxorubicin through reaction with its internal cysteines, then coupled to iRGD peptides to generate iRGD-PhMV-Aldox (Figure 4B). The final product was not substantially altered in its nanostructure as compared to PhMV VLPs or other iRGD-PhMV nanoparticles and was monodisperse and homogenous (Figure 4C-E, Figure S9A). Based on UV-Vis spectroscopy, ~70 doxorubicin molecules were conjugated per iRGD-PhMV-Aldox NP (Figure S9B-C). Owing to the labile nature of the hydrazone linker, a small amount of free doxorubicin was seen in some characterization methods and likely represents doxorubicin that is non-covalently contained within the PhMV nanoparticles, likely due to supramolecular π–π stacking of doxorubicin.

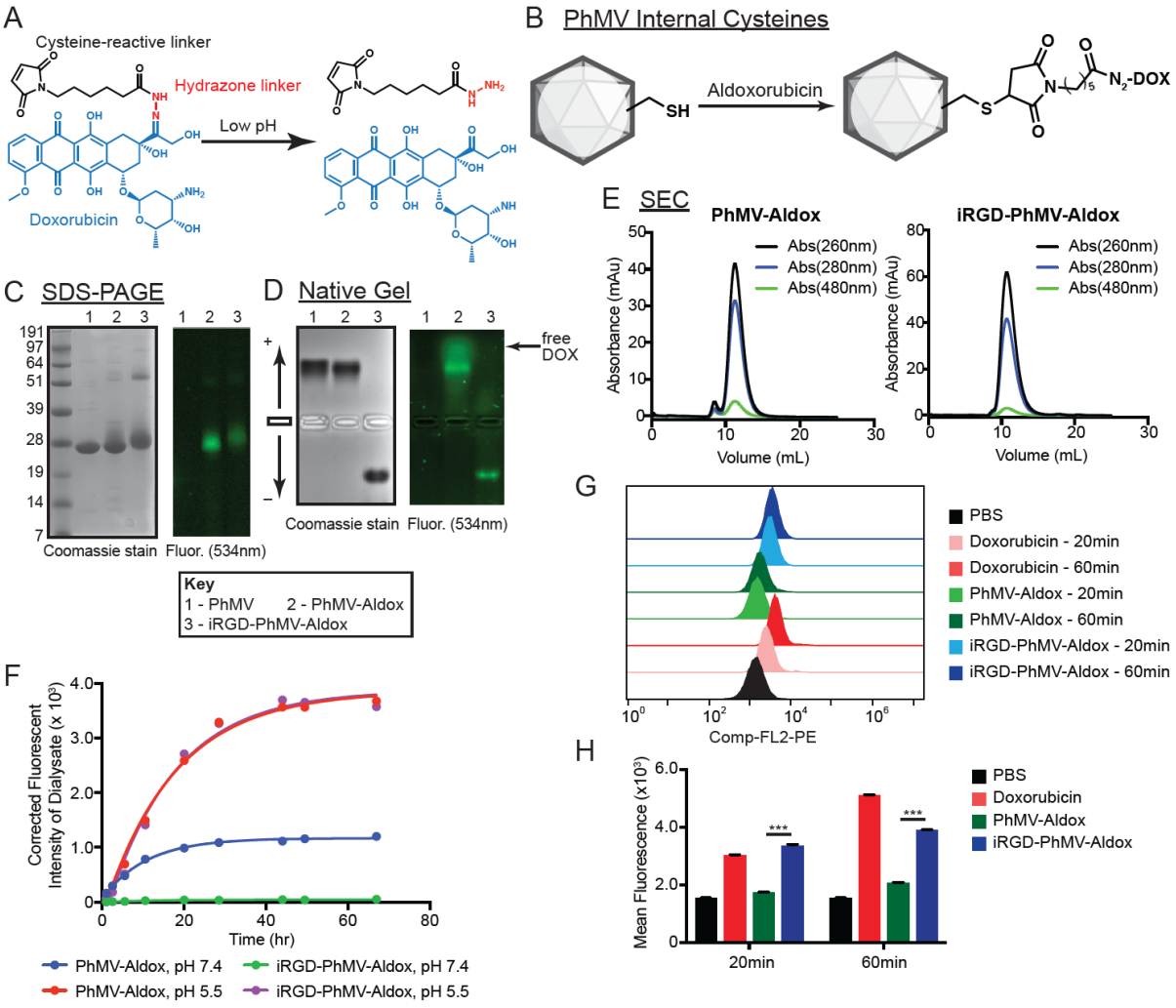

Figure 4. Synthesis and characterization of Aldoxorubicin-iRGD-PhMV conjugates. A. Chemical components of aldoxorubicin. B. Scheme for conjugation of aldoxorubicin to internal cysteines of PhMV. C-E. Characterization of PhMV-Aldox-iRGD and PhMV-Aldox using SDS-PAGE (C), native gel electrophoresis (D), and size exclusion chromatography (E). F. Fluorescent intensity of dialysate after dialysis of PhMV-Aldox or iRGD-PhMV-Aldox into PBS (pH 7.4) or 50mM Na citrate (pH 5.5) at 37ºC. G-H. iRGD-PhMV-Aldox and PhMV-Aldox uptake by A2780 cells after 20 and 60 minutes, as measured by flow cytometry (G) with quantification (H). Error bars represent S.E.M of three replicates. Statistical analysis by two-tailed t-test (***: $p<0.001$).

***In vitro* drug release and cytotoxicity of iRGD-PhMV-Aldox nanoparticles.** We next assessed if aldoxorubicin-conjugated PhMV nanoparticles functioned as expected *in vitro*. We observed that free doxorubicin is rapidly released from iRGD-PhMV-Aldox nanoparticles at low

pH (pH 5.5) but not at physiologic pH (Figure 4F), which indicates the hydrazone linker functions as expected. To assess if iRGD-PhMV-Aldox nanoparticles display increased cellular uptake, we performed flow cytometry. A2780 cells treated with iRGD-PhMV-Aldox showed a nine- and four-fold increase in internal fluorescence after 20 and 60 minutes, respectively, as compared to cells treated with PhMV-Aldox, indicative of increased cellular uptake of iRGD-PhMV-Aldox NPs (Figure 4G). The level of cellular uptake of iRGD-PhMV-Aldox was similar to that of free doxorubicin (Figure 4H). When treated with a similar absolute dose of doxorubicin, no significant difference in cytotoxicity is observed between iRGD-PhMV-Aldox and PhMV-Aldox, likely due to the long timescale of this assay (72hrs) (Figure S10).

***In vivo* efficacy of iRGD-PhMV-Aldox in murine cancer model.** To assess if iRGD-PhMV-Aldox nanoparticles show improved anti-tumor efficacy, we generated a PEG2Kylated version of these particles for *in vivo* studies (Figure S11). We then used a previously established MDA-MD-231 xenograft tumor model in Nu/Nu BALB/c mice. Once tumor volume reached ~100 mm^3, mice were treated twice weekly with iRGD-PEG2K-PhMV-Aldox, PEG2K-PhMV-Aldox coadministered with 4 μmol/kg free iRGD peptide, or PEG2K-PhMV-Aldox (Figure 5A). Nanoparticle dosing was normalized to deliver 0.5 mg doxorubicin per kg animal body weight. In the control (PBS) and PhMV-Aldox treatment arms, tumor volumes reached 1000 mm^3 after approximately 50-75 days (Figure S12A-B). Treatment with iRGD-PhMV-Aldox significantly reduced tumor volume and increased survival as compared to control (Figure 5B-C). In fact, four animals showed complete tumor regression at Day 136 (Figure S12C). Co-administration of PEG2K-PhMV-Aldox with free iRGD peptide significantly reduced tumor volume but did not

significantly alter survival (Figure S12D). Mouse weights were similar across all treatment groups (Figure 5D).

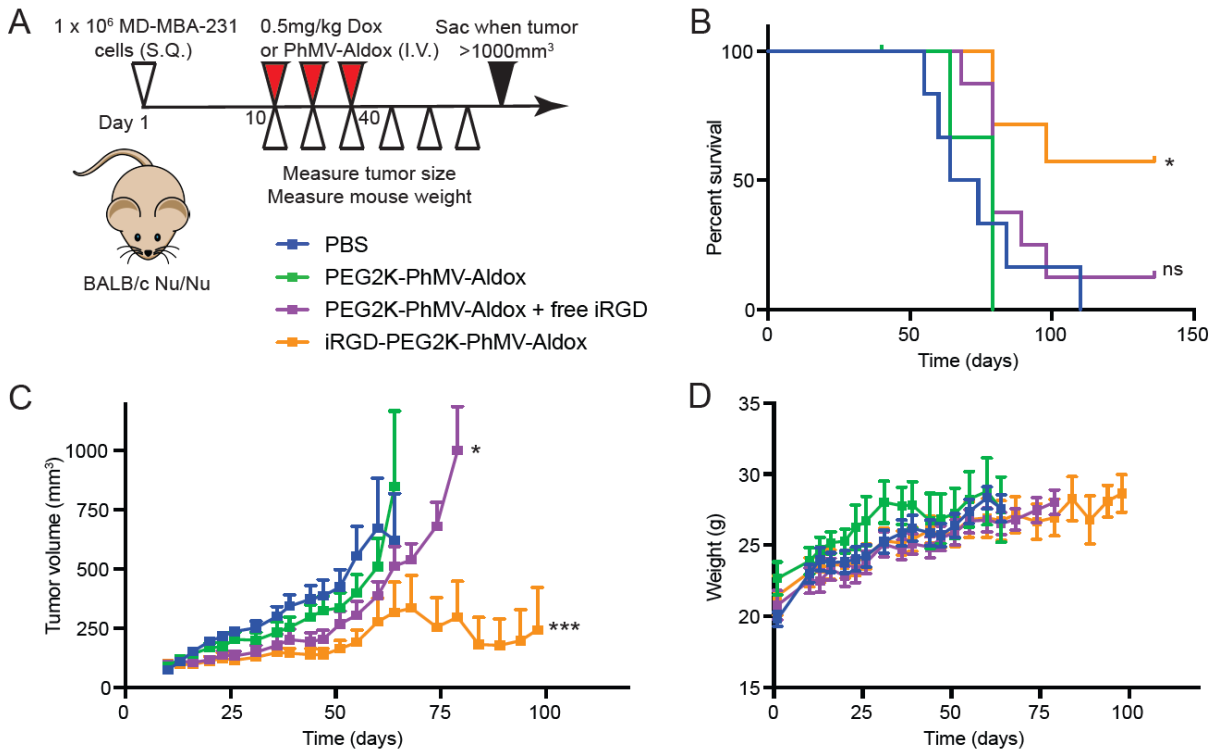

Figure 5. Inhibition of growth in an MDA-MB-231 xenograft model. A. MDA-MD-231 cells are injected sucutaneously into BALB/c Nu/Nu mice. Treatment began when tumors reached a voume of ~100mm3 and involved twice-weekly intravenous bolus of PBS, 0.5mg/kg doxorubicin, PEG2K-PhMV-Aldox, PEG2K-PhMV-Aldox + free iRGD (8mmol/kg), or iRGD-PEG2K-PhMV-Aldox. Treatment was stopped at day 40. B. Animals were sacrified when tumor volumes reached 1000mm3. Statistical analysis of survival curves were carried out by log-rank (Mantel-Cox) test, ns: $p>0.05$, *: $p<0.05$, as compared to PEG2K-PhMV-Aldox. C-D. Mean tumor volumes (C) and mean animal weights (D). Error bars represent the S.E.M. Statistical analysis was carried out by two-way ANOVA (*: $p<0.05$, ***: $p<0.001$, as compared to PEG2K-PhMV-Aldox).

Discussion and Conclusions

We have developed a novel iRGD-peptide conjugated virus-like nanoparticle for targeted cancer cell uptake. After identifying a strategy for the robust bioconjugation of iRGD peptides to PhMV nanoparticles (Figure 1), we show that iRGD-PhMV is rapidly taken up by cultured cancer cells

411 *in vitro* (Figure 2) and has increased intratumoral localization *in vivo* (Figure 3). We then show
412 that iRGD-PhMV can be loaded with the cytotoxic drug doxorubicin (Figure 4) and show that
413 iRGD-PhMV-Aldox shows improved anti-tumoral efficacy as compared to non-targeted control
414 (Figure 5).
415
416 By using click chemistry with propargylglycine-iRGD peptides and azide-functionalized PhMV,
417 we were able to vary the number of surface-bound iRGD peptides on iRGD-PhMV NPs. A four-
418 fold change in the stoichiometry of iRGD peptide used during conjugation led to a nearly 20-fold
419 increase in the αv integrin binding affinity of iRGD-PhMV NPs (Figure 2A-B). However,
420 increasing the biochemical affinity of multivalent nanoparticles for their target does not directly
421 increase on-target binding or specificity since increased ligands on NP surfaces can reduce
422 particle circulatory time and alter the mechanics of target engagement.[36] In fact, a reduction in
423 the density of anti-intercellular adhesion molecule-1 (ICAM-1) antibodies on the surface of
424 poly(4-vinylphenol) (PVPh) NPs was found to paradoxically increase the specificity of target
425 engagement.[37] This suggests that further characterization of iRGD-VLPs may be needed to
426 empirically determine the appropriate surface iRGD-peptide concentration to maximize tumor
427 homing properties.
428
429 Since plant viruses have not evolved to be infectious towards mammalian cells, plant viral NPs
430 and VLPs typically enter the cytoplasm of mammalian cells through passive endocytosis[38] or
431 interaction with highly evolutionarily conserved surface proteins, such as the interaction of
432 cowpea mosaic virus (CPMV) and other members of the picornavirus superfamily with
433 vimentin.[39,40] The rate of uptake of iRGD-PhMV that we observed in this study is significantly

higher than non-liganded PhMV (Figure 2C-D) and is approaching the rate of cellular entry for the small molecule doxorubicin (Figure 4G-H). This rate of cellular internalization, along with the punctate foci of iRGD-PhMV-Cy5 observed by confocal microscopy (Figure 2E), suggest active cellular uptake of iRGD-PhMV NPs. This may be due to αv integrin-mediated cellular uptake or activation of NRP-1-mediated micropinocytosis of the C-end rule (CendR) peptide that is revealed after proteolytic cleavage of iRGD-peptides.[25,41]

The similar degree of tumor localization of iRGD-PEG2K-PhMV-Cy5 and PEGK2K-PhMV-Cy5 co-administered with free iRGD peptide is consistent with prior work that showed similar tumor accumulation of 130nm nanoparticles consisting of albumin-embedded paclitaxel after conjugation to or co-administration with iRGD-peptide.[26] However we still observed significant non-specific uptake of PhMV NPs in the liver and spleen, despite surface shielding with PEG. The trend towards increased uptake of iRGD-PhMV NPs observed in the liver and kidney may be due to the native expression of *ITGA3* and *ITGA5*, which encode for β3 and β5 integrin subunits, in endothelial cells of these organs.[42] Further optimization of surface iRGD peptide concentration may provide a strategy to reduce these non-tumoral binding events, although it is likely that these will remain sites of non-specific uptake for all PhMV VLPs despite surface peptide targeting. Although hepatotoxicity has not been significantly observed in clinical trials of doxorubicin nanoparticles[43] or pre-clinical testing of doxorubicin-containing VLPs,[44] further work and efficacy studies of iRGD-PhMV-Aldox will be critical to ensure safety.

Since the tumoral delivery of PhMV-Cy5 was increased nearly 50% with iRGD-peptide co-administration or conjugation after 48 hours and because of the long tumoral residency time of

457 PhMV VLPs (Figure 3B), we hypothesized that multiple repeat administrations of iRGD-
458 conjugated PhMV-Aldox would result in a multiplicative increase in the delivery of doxorubicin
459 over time. As evidence of this, twice weekly dosing of 0.5 mg/kg doxorubicin by iRGD-PEG2K-
460 PhMV-Aldox particles is significantly more effective than delivery of the same dose by non-
461 targeted PEG2K-PhMV-Aldox particles (Figure 5). In fact, a complete response was observed in
462 4/7 animal treated with iRGD-PEG2K-PhMV-Aldox while none were observed with PEG2K-
463 PhMV-Aldox treatment. The reduced effect of co-administration of iRGD-peptide with
464 PEGK2K-PhMV-Aldox as compared to direct conjugation in this setting may be due to a
465 mismatch between the timing of the 'bystander effect,' which peaks 15-30 min after iRGD-
466 peptide administration[45] and the long serum half-life of PhMV VLPs.[19] Additionally, there could
467 be altered transit of iRGD-conjugated vs co-administered PhMV VLPs into the tumor
468 parenchyma. The low efficacy of non-targeted PEG2K-PhMV-Aldox is likely due to the low
469 dose of doxorubicin administered (0.5 mg/kg) compared to the recommended clinical dose of 60-
470 75 mg/m^2 or approximately 1.5 mg/kg in breast cancer combination therapy (Lexicomp, Inc.).
471 That a lower cumulative dose of doxorubicin is still efficacious when delivered as an iRGD
472 peptide-targeted nanoparticle suggests this method of drug deliver could be used to reduce
473 systemic toxicity of doxorubicin and perhaps other chemotherapeutics while maintaining on-
474 target potency.
475
476 Several prior studies have employed doxorubicin-loaded VLPs for targeted tumor delivery. The
477 direct intratumoral delivery of tobacco mosaic virus (TMV) discs conjugated to aldoxorubicin
478 showed increased efficacy in an intracranial xenograft model of glioblastoma as compared to
479 free doxorubicin[46] and our group has previously demonstrated that non-targeted PEG2K-PhMV-

Aldox VLPs display increased efficacy as compared free doxorubicin.[31] This work differs from these prior studies in the use of iRGD peptide-based targeting. Additionally, a prior study used genetic engineering to insert RGD peptides into the major immunodominant loop region (MIR) of hepatitis B core protein (HBc) VLPs and used disassembly-reassembly to encapsulate doxorubicin into the VLP[44]. Our work differs from this study in two regards. First, we use acid-labile conjugation of doxorubicin to PhMV VLPs, which adds an additional layer of specificity of tumoral delivery. Second, we use non-genetic strategies for RGD peptide-VLP conjugation, which allows for facile alterations in peptide:VLP stoichiometry, as demonstrated in Figure S2-S4, as well as the use of the more advanced iRGD peptide, which takes additional advantage of CendR-mediated tumoral uptake. Taken together, these data suggest that iRGD-PhMV VLPs hold high promise for the targeted delivery of chemotherapeutics and other small molecules to tumors after intravascular injection.

Author Contributions

K.J.B. and Z.Z. performed experiments. K.J.B. and N.F.S. designed and analyzed experiments. K.J.B. and N.F.S. wrote the manuscript.

Conflict of Interest

Dr. Steinmetz is a co-founder of, has equity in, and has a financial interest with Mosaic ImmunoEnginering Inc. Dr. Steinmetz serves as Director, Board Member, and Acting Chief Scientific Officer, and paid consultant to Mosaic. The other authors declare no potential COI.

Acknowledgements and Funding

We thank Dr. Kersi Pestonjamasp for assistance with confocal microscopy and all members of the Steinmetz lab for helpful discussions and critical review. This work was funded in part by the National Institutes of Health (NIH T32EB005970, to UCSD Dept. of Radiology; R01-CA202814 and R01-CA253615, to N.F.S.) and RSNA Research & Education Foundation, through grant number RR2251 (to K.J.B.). The content is solely the responsibility of the authors and does not necessarily represent the official views of the RSNA R&E Foundation.

References

1. Ahmad, F. B. & Anderson, R. N. The Leading Causes of Death in the US for 2020. *JAMA* **325,** 1829–1830 (2021).
2. Manzari, M. T. *et al*. Targeted drug delivery strategies for precision medicines. *Nat Rev Mater* **6,** 351–370 (2021).
3. Srinivasarao, M. & Low, P. S. Ligand-Targeted Drug Delivery. *Chem. Rev.* **117,** 12133–12164 (2017).
4. Shi, J., Kantoff, P. W., Wooster, R. & Farokhzad, O. C. Cancer nanomedicine: progress, challenges and opportunities. *Nat. Rev. Cancer* **17,** 20–37 (2017).
5. Zhao, Z., Ukidve, A., Kim, J. & Mitragotri, S. Targeting Strategies for Tissue-Specific Drug Delivery. *Cell* **181,** 151–167 (2020).
6. Wilhelm, S. *et al*. Analysis of nanoparticle delivery to tumours. *Nat Rev Mater* **1,** 1–12 (2016).
7. Blanco, E., Shen, H. & Ferrari, M. Principles of nanoparticle design for overcoming biological barriers to drug delivery. *Nat. Biotechnol.* **33,** 941–951 (2015).
8. Steinmetz, N. F. Viral nanoparticles as platforms for next-generation therapeutics and imaging devices. *Nanomedicine: Nanotechnology, Biology, and Medicine* **6,** 634–641 (2010).
9. Mitchell, M. J. *et al*. Engineering precision nanoparticles for drug delivery. *Nat Rev Drug Discov* **20,** 101–124 (2021).
10. Nkanga, C. I. & Steinmetz, N. F. The pharmacology of plant virus nanoparticles. *Virology* **556,** 39–61 (2021).
11. Rohovie, M. J., Nagasawa, M. & Swartz, J. R. Virus-like particles: Next-generation nanoparticles for targeted therapeutic delivery. *Bioeng Transl Med* **2,** 43–57 (2017).
12. Jeevanandam, J., Pal, K. & Danquah, M. K. Virus-like nanoparticles as a novel delivery tool in gene therapy. *Biochimie* **157,** 38–47 (2019).
13. Ma, Y., Nolte, R. J. M. & Cornelissen, J. J. L. M. Virus-based nanocarriers for drug delivery. *Adv Drug Deliv Rev* **64,** 811–825 (2012).

14. Azizgolshani, O., Garmann, R. F., Cadena-Nava, R., Knobler, C. M. & Gelbart, W. M. Reconstituted plant viral capsids can release genes to mammalian cells. *Virology* **441,** 12–17 (2013).
15. Shukla, S. & Steinmetz, N. F. Virus-based nanomaterials as positron emission tomography and magnetic resonance contrast agents: from technology development to translational medicine. *Wiley Interdiscip Rev Nanomed Nanobiotechnol* **7,** 708–721 (2015).
16. Gulati, N. M., Stewart, P. L. & Steinmetz, N. F. Bioinspired Shielding Strategies for Nanoparticle Drug Delivery Applications. *Mol Pharm* **15,** 2900–2909 (2018).
17. Sastri, M. *et al*. Assembly of physalis mottle virus capsid protein in Escherichia coli and the role of amino and carboxy termini in the formation of the icosahedral particles. *J. Mol. Biol*. **272,** 541–552 (1997).
18. Masarapu, H. *et al*. Physalis Mottle Virus-Like Particles as Nanocarriers for Imaging Reagents and Drugs. *Biomacromolecules* **18,** 4141–4153 (2017).
19. Hu, H. *et al*. Physalis Mottle Virus-like Nanoparticles for Targeted Cancer Imaging. *ACS Appl Mater Interfaces* **11,** 18213–18223 (2019).
20. Hanahan, D. & Weinberg, R. A. The hallmarks of cancer. *Cell* **100,** 57–70 (2000).
21. Carmeliet, P. Mechanisms of angiogenesis and arteriogenesis. *Nat. Med*. **6,** 389–395 (2000).
22. Bergers, G. & Benjamin, L. E. Tumorigenesis and the angiogenic switch. *Nat. Rev. Cancer* **3,** 401–410 (2003).
23. Zhao, Y. & Adjei, A. A. Targeting Angiogenesis in Cancer Therapy: Moving Beyond Vascular Endothelial Growth Factor. *Oncologist* **20,** 660–673 (2015).
24. Arap, W., Pasqualini, R. & Ruoslahti, E. Cancer treatment by targeted drug delivery to tumor vasculature in a mouse model. *Science* **279,** 377–380 (1998).
25. Sugahara, K. N. *et al*. Tissue-penetrating delivery of compounds and nanoparticles into tumors. *Cancer Cell* **16,** 510–520 (2009).
26. Sugahara, K. N. *et al*. Coadministration of a tumor-penetrating peptide enhances the efficacy of cancer drugs. *Science* **328,** 1031–1035 (2010).
27. Kitagawa, T. *et al*. RGD targeting of human ferritin iron oxide nanoparticles enhances in vivo MRI of vascular inflammation and angiogenesis in experimental carotid disease and abdominal aortic aneurysm. *J Magn Reson Imaging* **45,** 1144–1153 (2017).
28. Liu, X. *et al*. Tumor-penetrating peptide enhances transcytosis of silicasome-based chemotherapy for pancreatic cancer. *J. Clin. Invest*. **127,** 2007–2018 (2017).
29. Puig-Saus, C. *et al*. iRGD tumor-penetrating peptide-modified oncolytic adenovirus shows enhanced tumor transduction, intratumoral dissemination and antitumor efficacy. *Gene Ther* **21,** 767–774 (2014).
30. Schindelin, J. *et al*. Fiji: an open-source platform for biological-image analysis. *Nat. Methods* **9,** 676–682 (2012).
31. Hu, H. & Steinmetz, N. F. Doxorubicin-Loaded Physalis Mottle Virus Particles Function as a pH-Responsive Prodrug Enabling Cancer Therapy. *Biotechnol J* **15,** e2000077 (2020).
32. Rostovtsev, V. V., Green, L. G., Fokin, V. V. & Sharpless, K. B. A stepwise huisgen cycloaddition process: copper(I)-catalyzed regioselective 'ligation' of azides and terminal alkynes. *Angew Chem Int Ed Engl* **41,** 2596–2599 (2002).
33. Tornøe, C. W., Christensen, C. & Meldal, M. Peptidotriazoles on solid phase: [1,2,3]-triazoles by regiospecific copper(i)-catalyzed 1,3-dipolar cycloadditions of terminal alkynes to azides. *J. Org. Chem*. **67,** 3057–3064 (2002).

34. Suk, J. S., Xu, Q., Kim, N., Hanes, J. & Ensign, L. M. PEGylation as a strategy for improving nanoparticle-based drug and gene delivery. *Adv Drug Deliv Rev* **99,** 28–51 (2016).
35. Lebrecht, D. *et al*. The 6-maleimidocaproyl hydrazone derivative of doxorubicin (DOXO-EMCH) is superior to free doxorubicin with respect to cardiotoxicity and mitochondrial damage. *Int J Cancer* **120,** 927–934 (2007).
36. Howard, M. *et al*. Vascular targeting of nanocarriers: perplexing aspects of the seemingly straightforward paradigm. *ACS Nano* **8,** 4100–4132 (2014).
37. Zern, B. J. *et al*. Reduction of nanoparticle avidity enhances the selectivity of vascular targeting and PET detection of pulmonary inflammation. *ACS Nano* **7,** 2461–2469 (2013).
38. Cossart, P. & Helenius, A. Endocytosis of viruses and bacteria. *Cold Spring Harb Perspect Biol* **6,** a016972 (2014).
39. Koudelka, K. J. *et al*. Endothelial targeting of cowpea mosaic virus (CPMV) via surface vimentin. *PLoS Pathog*. **5,** e1000417 (2009).
40. Steinmetz, N. F., Cho, C.-F., Ablack, A., Lewis, J. D. & Manchester, M. Cowpea mosaic virus nanoparticles target surface vimentin on cancer cells. *Nanomedicine (Lond)* **6,** 351–364 (2011).
41. Pang, H.-B. *et al*. An endocytosis pathway initiated through neuropilin-1 and regulated by nutrient availability. *Nat Commun* **5,** 4904–12 (2014).
42. Karlsson, M. *et al*. A single-cell type transcriptomics map of human tissues. *Sci Adv* **7,** (2021).
43. Shafei, A. *et al*. A review on the efficacy and toxicity of different doxorubicin nanoparticles for targeted therapy in metastatic breast cancer. *Biomed Pharmacother* **95,** 1209–1218 (2017).
44. Shan, W. *et al*. Modularized peptides modified HBc virus-like particles for encapsulation and tumor-targeted delivery of doxorubicin. *Nanomedicine: Nanotechnology, Biology, and Medicine* **14,** 725–734 (2018).
45. Ruoslahti, E. Tumor penetrating peptides for improved drug delivery. *Adv Drug Deliv Rev* **110-111,** 3–12 (2017).
46. Finbloom, J. A. *et al*. Evaluation of Three Morphologically Distinct Virus-Like Particles as Nanocarriers for Convection-Enhanced Drug Delivery to Glioblastoma. *Nanomaterials (Basel)* **8,** 1007 (2018).